RSC Advances

ROYAL SOCIETY OF CHEMISTRY

PAPER

View Article Online
View Journal | View Issue

Cite this: *RSC Adv.*, 2026, **16**, 7252

Silver citrate engineered $NiCo_2S_4$/MOF-derived oxide@carbon frameworks for high-energy hybrid supercapacitors

Areeba Sajid,†[a] Mohsin Ali Marwat, †*[a] Hamza Mohsin,[a] Syed Shaheen Shah,[b] Muhammad Arqam Karim, [a] Muhammad Ramzan Abdul Karim, [a] Muhammad Tariq,[a] Zuhair Ehsan,[a] Anusha Arif[a] and Esha Ghazanfar[a]

Received 26th November 2025
Accepted 7th January 2026

DOI: 10.1039/d5ra09122e

rsc.li/rsc-advances

Metal–organic frameworks (MOFs) offer a versatile platform for designing high-performance supercapacitor electrodes, but their poor intrinsic conductivity and structural instability limit practical application. Here, we report an silver-citrate-modified $NiCo_2S_4$@calcined-MOF composite derived from a trimetallic NiCoZn-MOF template for hybrid supercapacitor electrodes. The parent NiCoZn-TPA MOF is first calcined to form a porous NiO/CoO/ZnO/carbon framework that provides mechanical robustness and enhanced conductivity. $NiCo_2S_4$ nanoparticles are then grown *in situ* on this scaffold, followed by the incorporation of silver-citrate to introduce additional redox-active sites and highly conductive Ag pathways. Structural and chemical characterization confirms the successful formation of a plate-like oxide-carbon framework uniformly decorated with $NiCo_2S_4$ and silver-citrate nanoparticles. The optimized composite (A4, 60 wt% $NiCo_2S_4$@calcined-MOFs/40 wt% silver-citrate) delivers a high specific capacity of ~836C g^{-1} at 0.5 A g^{-1} in 1 M KOH. An asymmetric device based on A4//activated carbon achieves an energy density of 94 Wh kg^{-1} at 577 W kg^{-1}, while maintaining high-rate capability and 82% capacitance retention after 5000 cycles with 98% coulombic efficiency. Dunn analysis reveals combined faradaic and capacitive contributions, highlighting the hybrid charge-storage behavior of this MOF-derived multicomponent electrode architecture.

1 Introduction

The widespread development of renewable energy technologies and the increasing demand for efficient and portable power sources have intensified research into efficient energy-storage solutions. These devices are indispensable for mitigating the intermittency of renewable energy sources and for facilitating advanced power electronics, electric vehicles, and smart grids. Efficient energy storage devices ensure a reliable power supply and contribute towards a sustainable, low-carbon future. Conventional capacitors store energy through electrostatic charge separation between two conductive plates and offer a fast charge–discharge rate.[1] However, their efficiency is limited by low energy density, which confines their application to instantaneous power balancing and short-term energy storage applications. Electrochemical energy storage systems, such as batteries, store energy through bulk faradaic redox reactions within the electrode materials, enabling high energy density and long-term storage stability. But they have limitations, including slow kinetics, degradation over repeated cycling, and safety risks associated with thermal instability. Supercapacitors represent a hybrid between traditional capacitors and batteries, combining electrostatic charge storage with redox reactions to offer high energy density, rapid power output, and high cycling stability.[2]

The charge-storage behavior of its electrodes directly influences the electrochemical performance of a supercapacitor. Based on their charge storage mechanisms, supercapacitors are categorized into electrical double-layer capacitors (EDLCs), pseudocapacitors, and hybrid supercapacitors.[3] Energy storage in EDLCs occurs because charges accumulate electrostatically at the electrode–electrolyte interface. This phenomenon is typically observed in carbonaceous materials such as graphene, activated carbon (AC), and carbon nanotubes (CNTs), as these materials offer high specific surface area, superior electrical conductivity, and stable cycling performance.[4] Pseudocapacitors, in contrast, store energy *via* reversible redox reactions of electroactive compounds, such as transition-metal compounds and conducting polymers (*e.g.*, polypyrrole, polyaniline), which play an important role in increasing specific capacitance through faradaic processes.[5] Numerous transition-

---

[a] *Department of Materials Science and Engineering, Ghulam Ishaq Khan (GIK) Institute of Engineering Sciences and Technology, Topi 23640, Pakistan. E-mail: mohsin.ali@giki.edu.pk; Fax: +92-938-281032; Tel: +92-938-281026*

[b] *Department of Material Chemistry, Graduate School of Engineering, Kyoto University, Nishikyo-ku, Kyoto 615-8520, Japan*

† These authors contributed equally to this work.

metal-based compounds have been investigated for their pseudocapacitive performance. Transition metal oxides exhibit high theoretical capacitance and structural robustness. Still, they are constrained by their limited electrical conductivity, whereas phosphates and phosphides possess multiple redox-active sites but undergo structural deterioration during extended cycling.[6] Transition metal selenides exhibit enhanced ion diffusion and redox activity owing to their larger ionic radii and lower electronegativity. However, their limited surface area and structural instability hinder long-term performance. Transition metal sulfides (TMS) demonstrate higher conductivity and richer redox activity but still require structural optimization to maintain long-term stability. To achieve superior energy and power performance, recent studies have targeted designing hybrid and composite electrode materials that combine the high conductivity and stability of carbon materials with the rich redox response of metal compounds and polymers.[7]

MOFs and their derivatives have risen to prominence in energy-storage research as high-performance precursors in the synthesis of efficient electrode materials. Their well-tailored porosity, high specific surface area, and uniformly distributed metal nodes provide an effective precursor for engineering electrode materials with controlled composition and morphology.[8] Their well-ordered crystalline structures allow precise modulation of the metal-to-ligand ratio and pore size, enabling the design of materials with optimized electrochemical properties. Despite this, MOFs are stabilized by coordination bonds formed between transition-metal centers and organic linkers.[9] In contrast to covalent or metallic bonds, these coordination interactions are relatively localized and weak, resulting in limited structural robustness during repeated electrochemical cycling, where ion insertion and extraction can induce framework distortion. Various approaches have been adopted to overcome these challenges, such as incorporating conductive additives, including carbon-based materials and conductive polymers, and the rational design of multi-metallic MOFs to enhance conductivity, structural robustness, and electrochemical performance.[10] For instance, M. A. Karim *et al.* reported that incorporating multiple metal centers within a MOFs framework (NiCoCu-TPA) significantly enhanced redox kinetics, electrical conductivity, and overall electrochemical performance compared to monometallic counterparts.[11] Similarly, NiCoMn MOFs integrated with silver-citrate and CNTs delivered a specific capacitance of 730 F g at 0.5 A g^{-1}, twice that of the pristine MOFs (370 F g^{-1}).[12] The conversion of MOFs into functional derivatives and their utilization as templates for the *in situ* growth of highly conductive phases, such as transition-metal sulfides, nitrides, or phosphides, have emerged as particularly effective approaches for reducing charge-transfer resistance and improving electrical conductivity, structural robustness, and cycling stability.[13] For instance, a ZrO_2/C nanocomposite was prepared by pyrolyzing MOFs. Its carbon matrix provided inherent conductivity, achieving 241.5 F g^{-1} at 1 A g^{-1}, while a solid-state symmetric supercapacitor delivered 29 Wh kg^{-1} at 1.5 kW kg^{-1} and retained 97% capacitance over 2000 cycles.[14]

In this work, trimetallic NiCoZn-MOFs were synthesized *via* hydrothermal synthesis and further calcined to yield a porous metal oxide-carbon framework. Calcination improved the structural stability of MOFs by forming metal oxides and increasing electrical conductivity by creating porous carbonaceous frameworks produced by the decomposition of organic linkers. The porous carbon framework provides a stable backbone that suppresses structural collapse while offering continuous charge transport pathways, thereby providing efficient ionic diffusion.[15] However, the conversion to oxides results in reduced specific capacitance due to the limited redox activity of oxide species.[16] To overcome this disadvantage, the calcined MOFs were used as a conductive framework for the *in situ* growth of $NiCo_2S_4$ nanoparticles.[17] TMS have garnered considerable attention due to their high electrical conductivity and the abundance of redox-active sites. Their lower sulfur electronegativity and higher metal–sulfur covalency promote enhanced charge-transfer kinetics, while multiple oxidation states of transition metals provide reversible redox behavior and high specific capacitance.[18] However, their performance is limited by particle pulverization caused by volume expansion during cycling, which compromises structural stability. Moreover, their inherently low porosity restricts electrolyte ion access, leading to capacity fading.[19] The porous carbon-metal oxide framework provides a robust and porous template for the uniform anchoring of sulfide nanoparticles, thereby enhancing electrical conductivity, enriching redox-active sites, and facilitating efficient ion diffusion.[20] Furthermore, the $NiCo_2S_4$@Calcined MOFs composite was integrated with silver-citrate to introduce additional redox activity and further boost overall electrochemical performance. Silver-based compounds are desirable due to their exceptional electrical conductivity and potential pseudocapacitive behavior. The excellent electrical conductivity of silver ions enables fast electron transport within the electrode, thus lowering charge-transfer resistance.[21] Simultaneously, the redox activity of Ag^+ provides additional pseudocapacitance, complementing the faradaic processes of the transition-metal sulfides.[22] Moreover, the citrate ligand enhances structural stabilization, thereby improving electrochemical stability.[23] Therefore, the resulting $NiCo_2S_4$@-Calcined-MOFs/silver-citrate composite integrates the pseudocapacitive performance of transition-metal sulfides with the robust porous conductive template of MOFs-derived carbon. Additionally, incorporating silver citrate enhances electrical conductivity and pseudocapacitive behavior.

Despite extensive work on MOF-derived electrodes, three key gaps remain: (i) limited exploration of trimetallic MOF templates that are first transformed into robust oxide-carbon frameworks, (ii) insufficient use of such frameworks as conductive, porous hosts for transition-metal sulfides, and (iii) almost no integration of silver-citrate chemistry as a dual-function component that enhances both conductivity and pseudocapacitance. In this work, we address these gaps by designing an silver-citrate-incorporated $NiCo_2S_4$@calcined NiCoZn-MOF composite, where the calcined MOF provides a porous oxide-carbon backbone for *in situ* $NiCo_2S_4$ growth and subsequent silver-citrate incorporation. This multicomponent architecture maximizes the number of accessible redox-active sites, facilitates rapid ion and electron transport, and stabilizes the electrode during cycling. The optimized composition (A4) achieves a high specific capacity of 836C g^{-1} (0.5 A g^{-1}) and, in an A4//AC asymmetric configuration, delivers an energy density of 94 Wh kg^{-1} at 577 W kg^{-1} with 82% capacitance retention after 5000 cycles. These results demonstrate a scalable and straightforward strategy to couple MOF-derived oxide-carbon frameworks with transition-metal sulfides and silver-citrate, and they open a route to further performance improvements *via* compositional tuning and extension to other MOF and metal–ligand systems.

2 Methodology

2.1 Materials

Cobalt(II) nitrate hexahydrate ($Co(NO_3)_2 \cdot 6H_2O$, ≥98%), nickel(II) nitrate hexahydrate ($Ni(NO_3)_2 \cdot 6H_2O$, ≥98%) and zinc(II) nitrate hexahydrate ($Zn(NO_3)_2 \cdot 6H_2O$, ≥98%), silver nitrate ($AgNO_3$), terephthalic acid (TPA, $C_6H_4(COOH)_2$, ≥98%), sodium hydroxide (NaOH), sodium sulfide nonahydrate ($Na_2S \cdot 9H_2O$, ≥99.99%), potassium hydroxide (KOH, 99.995%), acetylene black (AB, 98%), and polyvinylidene fluoride (PVDF; Mn ≈ 534 000, GPC) were purchased from Sigma-Aldrich. Sodium citrate ($Na_3C_6H_5O_7$) was purchased from Honeywell (Germany), and nickel foam (Goodfellow, UK) was used as the current collector. *N*,*N*-dimethylformamide (DMF, ≥99%) and *N*-methyl-2-pyrrolidone (NMP, 99.5%) were precured from Sigma-Aldrich, while ethanol (C_2H_6O, ≥99.5%) and acetone (≥99.5%) were supplied by Merck and used as solvents during synthesis.

2.2 Synthesis of NiCoZn-TPA MOFs

For the preparation of the trimetallic MOFs, a metal precursor solution was first prepared by dissolving 5 mmol of each metal nitrate salt $Ni(NO_3)_2 \cdot 6H_2O$, $Co(NO_3)_2 \cdot 6H_2O$, and $Zn(NO_3)_2 \cdot 6H_2O$ in 30 mL of DMF under continuous stirring until all salts were completely dissolved as shown in Fig. 1. Upon dissolution, the metal salts dissociate to yield Ni^{2+}, Co^{2+}, and Zn^{2+} ions. This occurs because DMF, a polar aprotic solvent with a strong dipole moment, stabilizes the metal cations through ion–dipole interactions.[24] The carbonyl oxygen of DMF interacts electrostatically with the positively charged metal ions, while the nitrate anions and water molecules remain solvated, yielding a clear, stable metal precursor solution.[25] In a separate step, 7.5 mmol of TPA was dissolved in 20 mL of DMF to prepare the ligand solution. The solution was stirred for 30 minutes to ensure complete dissolution and uniform dispersion of TPA molecules. Thereafter, the ligand solution was added dropwise to the metal precursor solution under continuous stirring to facilitate effective coordination between the metal ions and TPA linkers. The reaction mixture was initially sonicated using a probe for 30 minutes to ensure uniform dispersion of the reactants and then subjected to solvothermal treatment at 160 °C for 24 hours in an autoclave. Under these conditions, DMF served both as the solvent and a mild base *via* thermal decomposition to dimethylamine, facilitating the deprotonation of the TPA ligand and complete coordination to metal ions. This process led to the self-assembly of a three-dimensional NiCoZn-TPA MOFs framework. The synthesized product was centrifuged with DMF to separate unreacted linker molecules. It was then centrifuged with de-ionized water and ethanol to remove unreacted precursors and impurities. The synthesized sample was then vacuum dried at 70 °C for 12 hours to facilitate the complete removal of residual solvent while preserving the structural integrity of the framework.

2.3 Calcination of MOFs

The dried MOF particles were placed in a ceramic crucible with a loosely fitted lid and calcined in a box furnace under controlled airflow of 1.0 L min^{-1}. This controlled atmosphere allowed partial oxidation of the organic linker while retaining a conductive carbonaceous matrix. The system was ramped from ambient temperature to 350 °C at a heating rate of 2 °C min^{-1} and held at 350 °C for 1 hour to initiate the transformation of terephthalate linkers into a carbonaceous matrix, minimizing structural collapse.[26] The temperature was then raised to 500 °C with the same heating rate and held for 2 h to complete the thermal conversion. During this stage, the metal centers were oxidized to form NiO, CoO, and ZnO. The prolonged time results in the formation of oxide, enhancing the structural stability of the calcined material.[27–29] The decomposition of the organic framework yielded a porous structure containing residual carbon from linker degradation, thereby improving electrical conductivity. The sample was then furnace-cooled, consisting primarily of NiO, CoO, and ZnO dispersed within a residual carbon matrix.

2.4 Synthesis of $NiCo_2S_4$@MOFs composites

$NiCo_2S_4$ nanoparticles were grown *in situ* on the calcined MOFs to form the $NiCo_2S_4$@MOFs composite, abbreviated as A1. For this, 100 mg of the calcined MOFs, used as a template, was dispersed in 40 mL of de-ionized water *via* probe sonication for 20 minutes. Separately, stoichiometric amounts according to 1 : 1.5 (calcined MOFs : Sulfide) of $Ni(NO_3)_2 \cdot 6H_2O$, $Co(NO_3)_2 \cdot 6H_2O$, and $Na_2S \cdot 9H_2O$ were dissolved in de-ionized water to prepare the precursor solution for $NiCo_2S_4$ formation. The precursor solution was then added to the MOFs dispersion, followed by probe sonication for 30 minutes to ensure homogeneous mixing. The resulting mixture was introduced into an autoclave and treated hydrothermally at 120 °C for 8 hours. After hydrothermal synthesis, the composite particles were centrifuged with de-ionized water and ethanol and vacuum-dried at 60 °C for 12 hours to prevent oxidation.[30]

2.5 Synthesis of silver-citrate

Silver-citrate was synthesized through a co-precipitation method using silver nitrate and trisodium citrate under mildly alkaline conditions to promote efficient coordination between silver and citrate ions, as shown in Fig. 1. For this, 6 mmol of $AgNO_3$ was dissolved in 50 mL of de-ionized water under continuous magnetic stirring at 500 rpm and 100 °C. The solution temperature was maintained at 100 °C to facilitate uniform nucleation. Separately, 2 mmol of $Na_3C_6H_5O_7 \cdot 2H_2O$ and 0.2 mmol of NaOH were dissolved in 30 mL of de-ionized

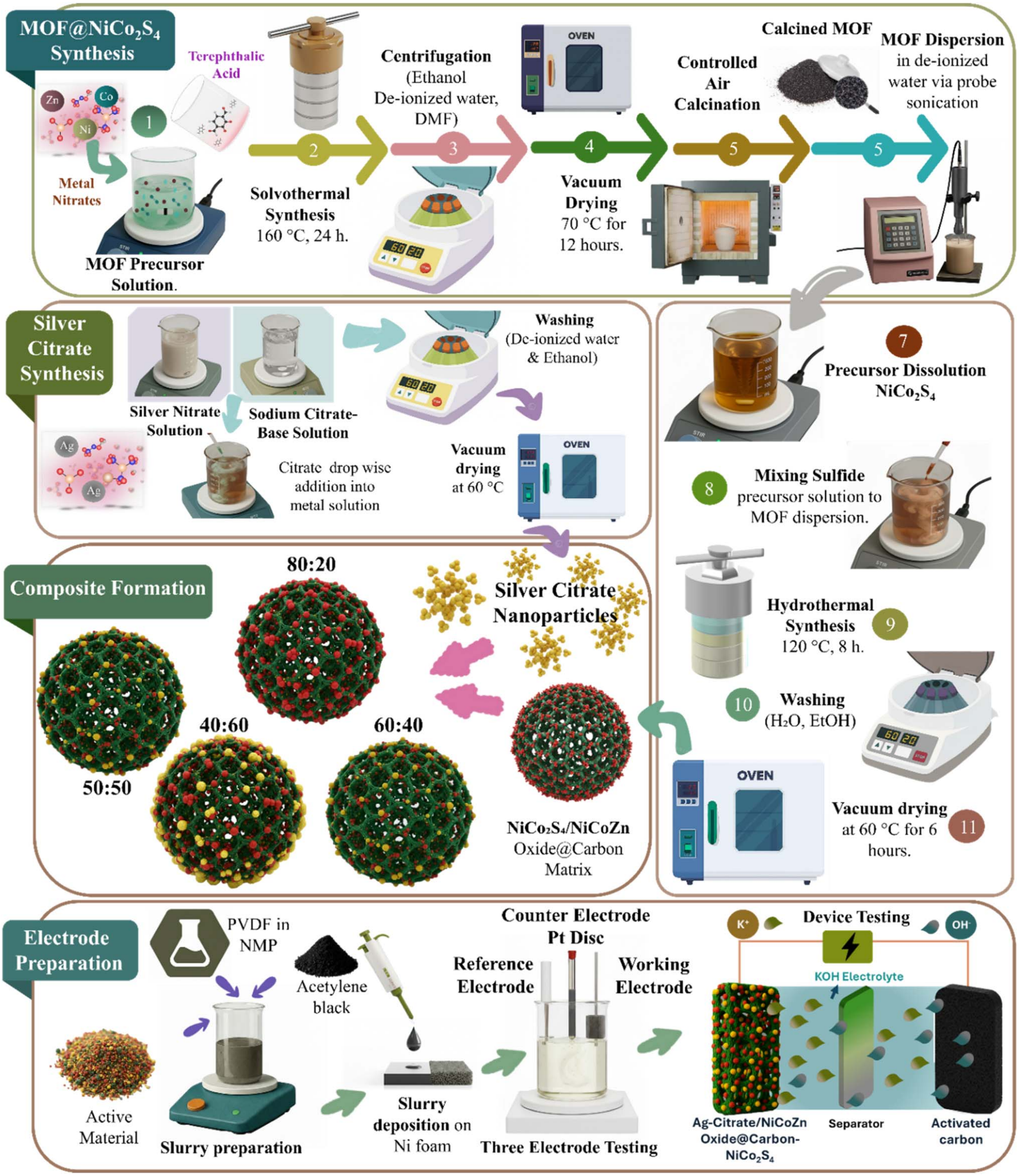

Fig. 1 Schematic illustration of the synthesis pathway, including: (i) preparation of the NiCoZn-MOF, (ii) calcination to obtain a metal-oxide and carbonaceous framework, (iii) *in situ* growth of NiCo$_2$S$_4$ on the calcined structure, (iv) integration of silver-citrate into the composite and (v) preparation of working electrode for electrochemical analysis.

water under stirring at room temperature until a clear solution was obtained. The addition of NaOH ensured complete deprotonation of sodium citrate to $C_6H_5O_7^{3-}$ ions, ensuring efficient coordination with Ag^+ ions. The pH of this solution was maintained between 8.0 and 9.0 (verified using pH paper) to suppress the formation of silver oxide or metallic silver. The citrate-based solution was then added dropwise into the hot $AgNO_3$ solution under continuous stirring. As the reactants were combined, the mixture changed from milky white to brown, confirming the formation of silver-citrate precipitate. To ensure full

Table 1 Compositional overview of the synthesized samples

Electrode material	% of $NiCo_2S_4$@Calcined metal organic framework	% of silver-citrate
A1	100	0
A2	0	100
A3	80	20
A4	60	40
A5	50	50
A6	40	60

precipitation, the mixture was maintained under stirring at 100 °C for 10 minutes. The reaction product was collected *via* centrifugation with de-ionized water at 6000 rpm for 10 minutes to eliminate residual ions and by-products (*e.g.*, $NaNO_3$ and NaOH). Finally, the purified silver-citrate was vacuum dried at 100 °C for 12 h to prevent photoreduction of Ag^+ to metallic silver.

2.6 Composite formation

To investigate the effect of silver-citrate incorporation on charge storage characteristics and electrochemical efficiency, a series of $NiCo_2S_4$@calcined-MOF/silver-citrate composites was prepared by varying the silver-citrate content. The pristine $NiCo_2S_4$@MOFs composite (A1) was used as the base material, while silver-citrate was introduced at different weight percentages through physical blending in mortar pastel, as shown in Table 1.

2.7 Electrode preparation for electrochemical measurements

Separate homogeneous slurries were prepared for each synthesized material (A1–A6) by combining the active material with AB and PVDF in a weight ratio of 80 : 10 : 10 in NMP as the solvent, as shown in Fig. 1. The mixtures were magnetically stirred at 200 rpm for 8 h to ensure uniform dispersion. The prepared slurry was drop-cast onto pre-cleaned Ni foam substrates and dried at 70 °C for 8 h, ensuring thorough solvent evaporation. Electrochemical analyses were performed in a three-electrode setup, using the prepared electrodes as the working electrode, a platinum disc as the counter electrode, and a Hg/HgO electrode as the reference electrode, in 1 M KOH aqueous solution as the electrolyte. The electrochemical performance of the electrodes was analyzed through cyclic voltammetry (CV), galvanostatic charge–discharge (GCD), and electrochemical impedance spectroscopy (EIS). For device assembly, the MOF-derived composite with silver citrate was employed as the positive electrode, while AC was used as the negative electrode. The AC electrode was prepared following the same procedure discussed above. A two-electrode configuration was constructed using A4||AC device assembly and Hoffman filter paper as the separator. The assembled device was subsequently subjected to electrochemical testing to evaluate its charge storage performance and long-term stability.

3 Characterization

The morphological, structural, and electrochemical characteristics of the pristine MOF-sulfide composite, silver-citrate, and their derived composite nanoparticles were comprehensively evaluated. The surface morphology, elemental composition, and dispersion in the synthesized samples were examined using scanning electron microscopy (SEM) coupled with energy-dispersive X-ray spectroscopy (EDX) (Carl Zeiss EVO 15, Jena, Germany). SEM analysis was performed at 8.49 mm working distance with an accelerating voltage of 15 kV at magnifications (1 kx to 50 kx). The samples for analysis were prepared by dispersing a small amount of the powdered material in de-ionized water, followed by ultrasonication to obtain a uniform suspension. A few drops of the resulting dispersion were then carefully placed onto a clean glass slab for subsequent examination. To minimize charging effects, samples were sputtered with a thin gold layer. X-ray diffraction (XRD) patterns were recorded using a PerkinElmer Spectrum Two 95 120 (Llantrisant, UK), while Fourier transform infrared (FTIR) spectra were obtained using a Bruker Alpha Platinum ATR system (New Jersey, USA). XRD measurements were performed with Cu Kα radiation ($\lambda = 1.5418$ Å) in the 2θ range of 10°–90°. FTIR spectra were collected in the range of 400–4000 cm^{-1} with a spectral resolution of 2 cm^{-1}. Electrochemical measurements, including three-electrode and device testing, were conducted using a Gamry Reference 3000 Potentiostat (Warminster, PA, USA) in 1 M KOH aqueous solution.

3.1 Structural characterization

XRD analysis results of the synthesized samples (A1–A6) is depicted in Fig. 2 showing the formation of the NiCoZn oxide-carbon matrix and the subsequent *in situ* growth of $NiCo_2S_4$, as well as the incorporation of silver-citrate in composites A3-A6. The sample A1 represents the MOF-derived NiCoZn Oxide@Carbon matrix, which serves as the structural template for $NiCo_2S_4$ growth. The diffraction peak observed at 43° is indexed to the (101) plane and represents the carbonaceous framework formed from the decomposition of the organic linker during calcination.[31–33] Distinct reflections appearing at 20.3° and 36.5° correspond to the (111) and (101) planes of CoO (JCPDS no. 65-5474).[31,34] The reflections appearing at 62.8° and 75.4° can be indexed to the (220) and (311) planes of NiO (JCPDS no. 47-1049),[35] while those observed at 31.7°, 47.7°, and 56.5° originates from the (100), (102), and (110) planes of ZnO (JCPDS no. 36-1451).[36] The simultaneous presence of these characteristic reflections confirms the successful formation of the metal oxide framework supported by the carbonaceous matrix. Diffraction peaks appearing at 16.3°, 26.6°, 27.2°, and 47.5° are indexed to the (111), (220), (220), and (311) planes of $NiCo_2S_4$ (JCPDS no. 20-0782), confirming the successful *in situ* growth of the sulfide phase on the calcined MOFs.[37,38]

Sample A2 exhibits peaks at 38.1°, 44.5°, 64.6°, and 77.7°, which correspond to the (101), (200), (220), and (311) planes, denoting the diffraction patterns of silver citrate (JCPDS no. 04-0783).[39,40] All composites display the characteristic peaks of the pristine A1 sample, while additional peaks associated with silver-

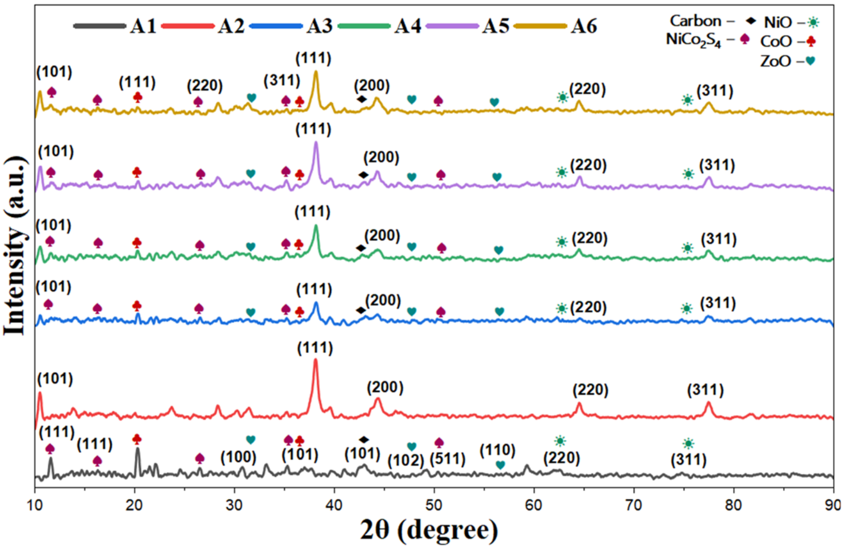

Fig. 2 The XRD patterns of samples (A1–A6) confirm the successful formation of the NiCoZn oxide@carbon matrix and the subsequent growth of $NiCo_2S_4$, along with the incorporation of silver-citrate in the composite structure.

citrate become progressively more pronounced from A3 to A6, reflecting the increasing silver-citrate percentage in these composites. Conversely, the relative intensity of A1-associated signals gradually decreases as higher silver-citrate ratios are incorporated. Collectively, these diffraction features confirm the successful formation of the designed NiCoZn-based composites with silver-citrate incorporation, verifying the coexistence of multiple crystalline phases within the electrode materials. The presence of unidentified peaks may be attributed to minor impurities, which are frequently observed in nano-synthesis.

Fig. 3 displays the FTIR spectra of samples A1–A6, highlighting the characteristic vibrational modes associated with the sample's structures. In sample A1, the FTIR spectrum displays the characteristic features of both the calcined MOFs and $NiCo_2S_4$, confirming their successful integration. The band at 1065 cm^{-1} corresponds to $NiCo_2S_4$ vibrations, while the 600 cm^{-1} peak arises from M–O stretching in the calcined Ni–Co–Zn oxide framework.[41] In sample A2, a broad absorption band at 3435 cm^{-1} appeared due to O–H stretching vibrations.[42] Vibrations associated with the asymmetric and symmetric stretching modes of the citrate carboxylate groups appear at 1517 cm^{-1} and 1382 cm^{-1}, respectively.[41] Additional features include C–H stretching vibrations between 780 cm^{-1} and 850 cm^{-1}, and C–O stretching bands at 1036 cm^{-1} and

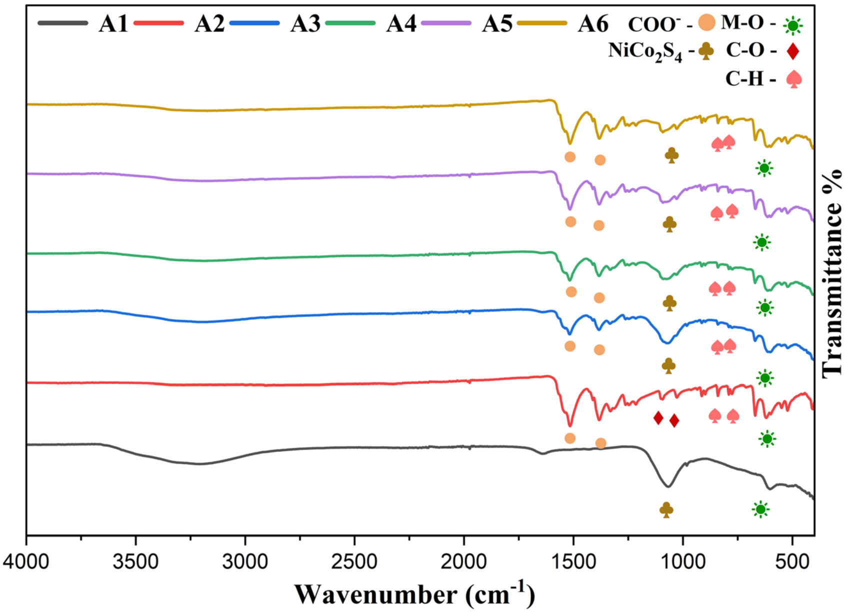

Fig. 3 The FTIR spectra of samples A1–A6 verify the successful formation of the NiCoZn oxide-carbon matrix with *in situ* grown $NiCo_2S_4$, and the subsequent incorporation of silver-citrate within the composite.

1090 cm^{-1}, confirming the presence of the citrate ligand.[43] All composites exhibit these characteristic peaks, with their relative intensities varying according to the proportion of pristine sample A1 and the amount of incorporated silver-citrate.

3.2 Morphological analysis

SEM was employed to visualize the *in situ* growth of sulfide particles and their incorporation into the calcined MOF-sulfide framework with silver-citrate nanoparticles. For sample A1 (Fig. 4(a1–c1)), the SEM images illustrates plate-like calcined MOF, on which *in situ*-generated sulfide nanoparticles are uniformly distributed, confirming effective surface nucleation and growth of sulfide nanoparticles on the calcined MOF substrate.[44] The EDX mapping of A1, as shown in Fig. 4(d1–i1), demonstrates a homogeneous distribution of Ni, Co, Zn, C, and O, confirming the presence of MOF-derived metal oxides and the *in situ* grown sulfide nanoparticles. The relatively higher concentrations of oxygen and carbon further support the contribution of the calcined MOFs framework to the composite. Additionally, the presence of S originating from $NiCo_2S_4$ verifies

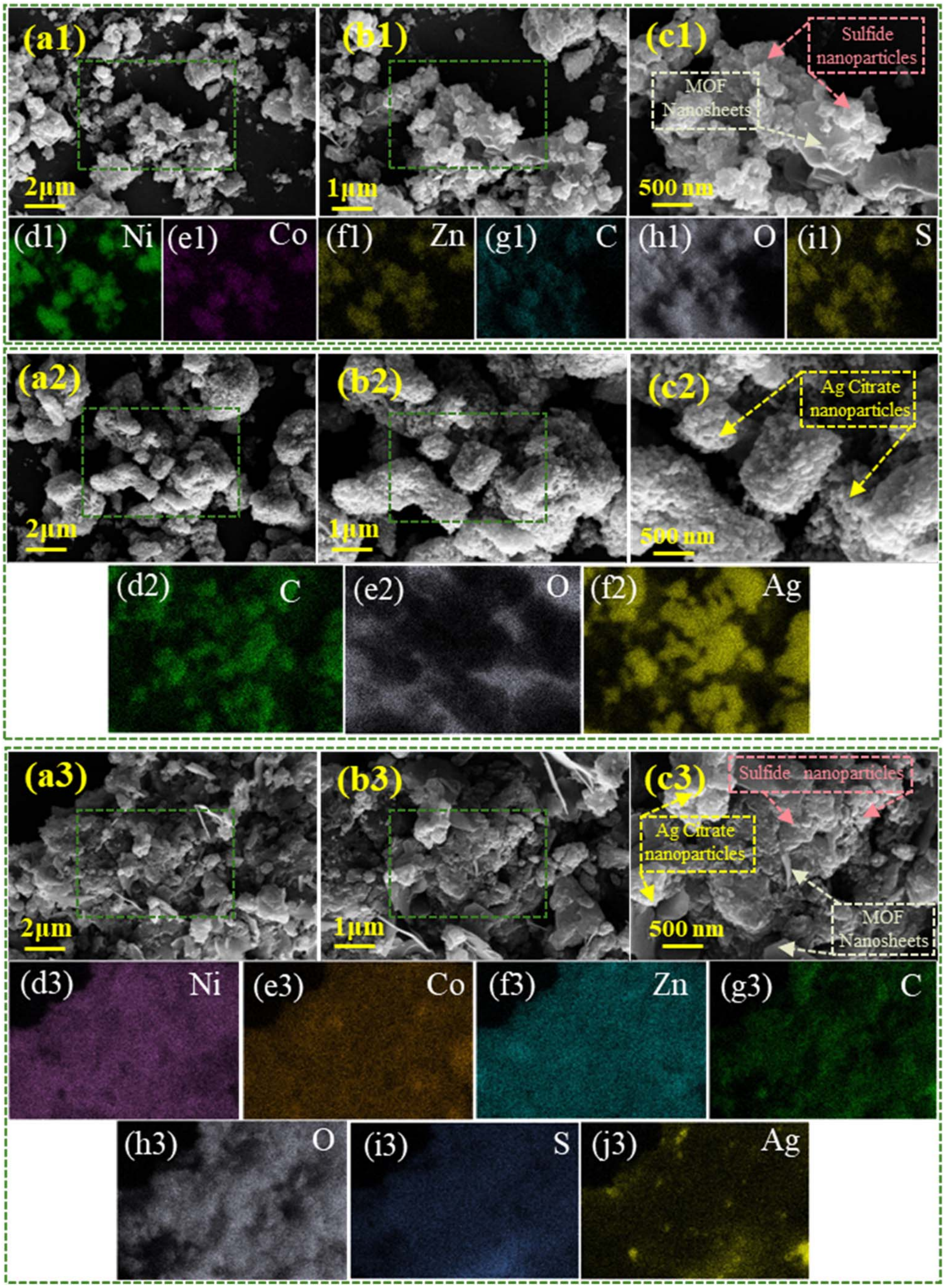

Fig. 4 SEM images at different magnifications along with EDX elemental mapping: A1 (a1–i1) pristine NiCoZn oxide@carbon-$NiCo_2S_4$, A2 (a2–e2) silver-citrate, and A4 (a3–j3) $NiCo_2S_4$@calcined MOF/silver-composite.

the coexistence of both the carbonaceous/metal-oxide matrix and the *in situ* formed sulfide phase. This elemental distribution aligns well with the interconnected morphology observed in the SEM images.

Sample A2 shown in Fig. 4(a2–c2) exhibits the microstructure of silver-citrate particles, which display a predominantly spherical-like geometry.[45] The EDX mapping of A2 Fig. 4(e2 and f2) shows a homogeneous distribution of C, O, and Ag, consistent with the composition of silver-citrate and confirming the uniform presence of Ag within the organic citrate matrix. Sample A5 SEM image as depicted in Fig. 4(a3–c3) reveals that the sheet-like calcined MOFs-sulfide framework serves as

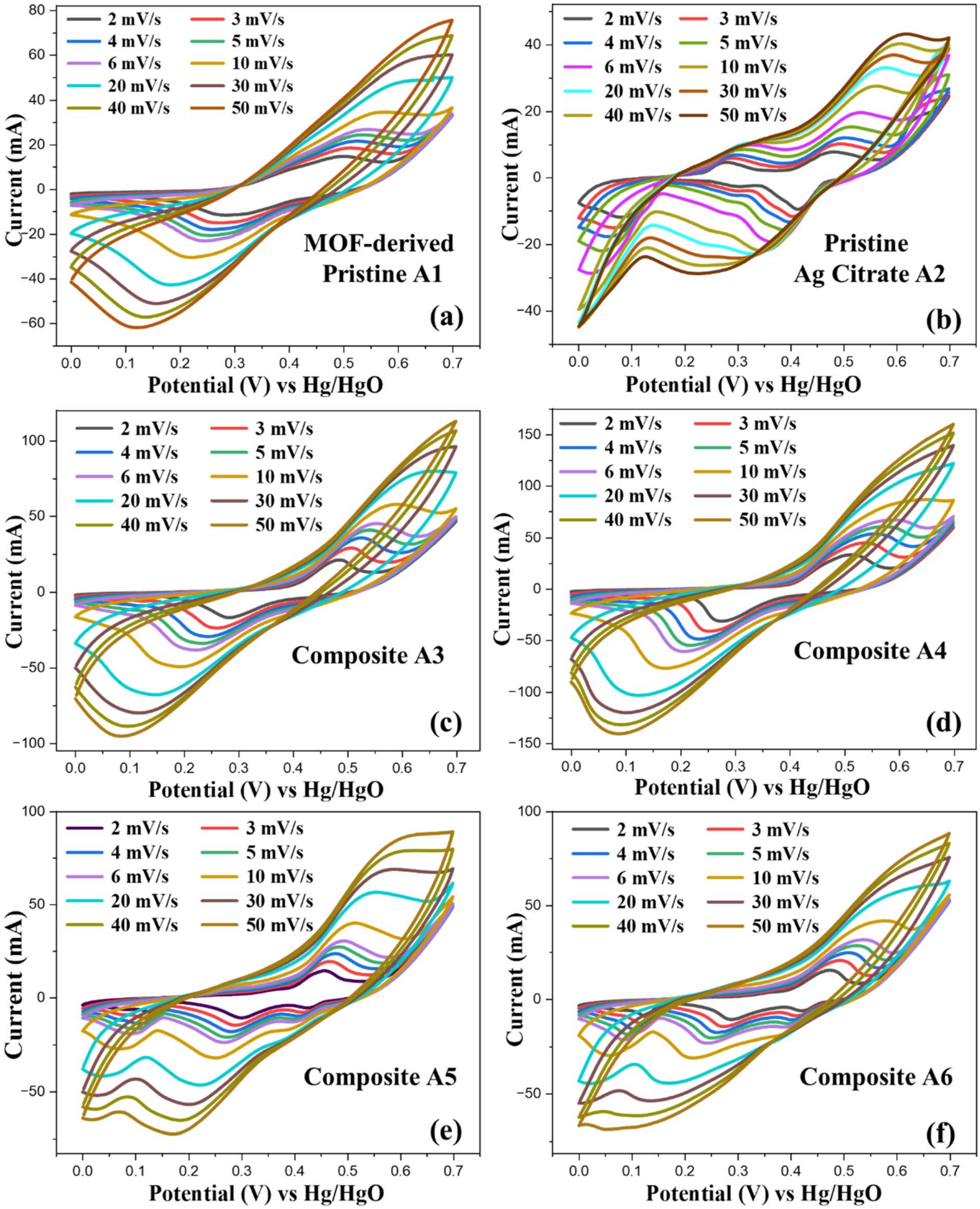

Fig. 5 CV curves of (a) A1, (b) A2, (c) A3, (d) A4, (e) A5 and (f) A6 at 0–0.7 V potential range with scan rates from 2 to 50 mV s^{-1}.

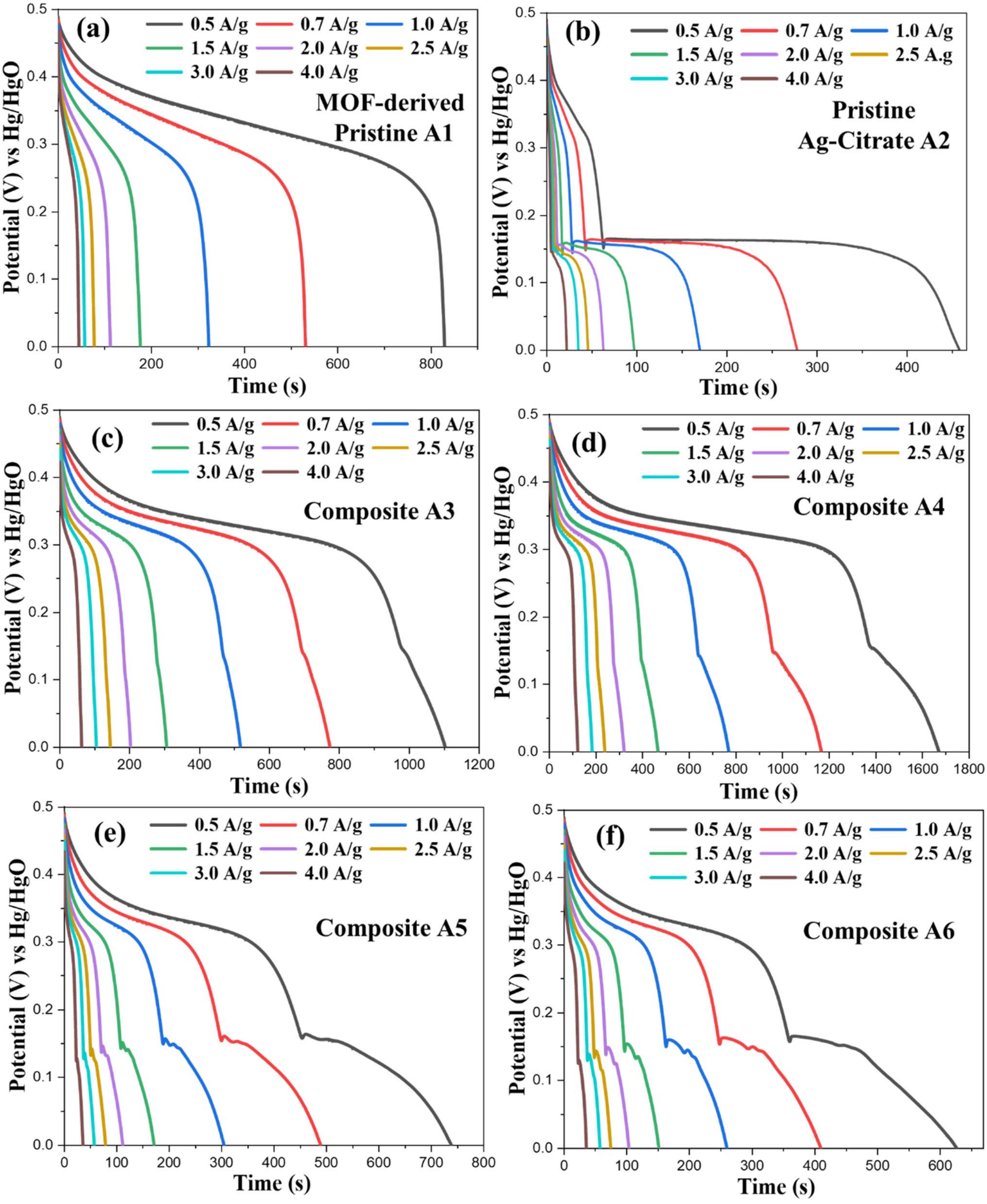

Fig. 6 GCD curves of samples (a) A1, (b) A2, (c) A3, (d) A4, (e) A5 and (f) A6 at 0.5–4 A g^{-1} current densities within 0–0.5 V, showing reversible faradaic redox behavior and the influence of silver-citrate incorporation on charge storage performance.

a template for the uniform anchoring of spherical silver-citrate nanoparticles. This configuration results in an interconnected network where silver-citrate particles are homogeneously dispersed across the sulfide-decorated calcined MOFs surface. The synergy among the calcined MOF, sulfide, and silver-citrate phases enhances electronic conductivity and facilitates efficient charge transport throughout the composite. The EDX mapping of A5, as illustrated in Fig. 4(d3–j3) confirms the coexistence of all constituent elements, showing a uniform distribution of Ni, Co, Zn, C, O, S, and Ag across the composite. The presence of Ni, Co, Zn, C, O, and S verifies the calcined MOF-sulfide framework, while the distinct Ag signals confirm the successful incorporation and homogeneous dispersion of silver-citrate nanoparticles. This elemental uniformity further supports the synergistic integration of the MOF-derived matrix, *in situ*-grown sulfides, and Ag particles, as evidenced by SEM morphology.

3.3 Electrochemical characterization

3.3.1 Three electrode testing. The electrochemical charge storage behavior of the prepared electrodes were evaluated through CV, at scan rates (2 to 50 mV s^{-1}) within 0–0.7 V potential in 1 M KOH aqueous solution. Sample A1, as shown in Fig. 5(a), exhibited pronounced oxidation–reduction peaks that intensified systematically with increasing scan rate, confirming the predominance of a faradaic pseudocapacitive mechanism. These redox features indicate the reversible Ni^{2+}/Ni^{3+} and Co^{2+}/Co^{3+} transitions, coupled with OH^- intercalation within the electrode material.[46] The proportional rise in current response with scan rate, along with a sustained CV curve shape over the entire potential window, indicates rapid charge-transfer kinetics due to the sulfide phase and efficient ionic diffusion within the porous framework of the calcined MOF. The CV profile of Sample A2, as illustrated in Fig. 5(b), exhibits two pairs of anodic and cathodic peaks, indicating multiple redox transitions. A broad set of redox peaks appears within 0.2–0.5 V, while an additional anodic peak emerges above 0.5 V and a cathodic peak below 0.2 V. The presence of these distinct redox couples reflects the simultaneous occurrence of several electrochemical processes associated with both silver ions transitions, along with an EDLC contribution from the citrate species.[47] Sample A3 (Fig. 5(c)) exhibited the characteristic redox peaks of the pristine $NiCo_2S_4$ (Sample A1), while simultaneously

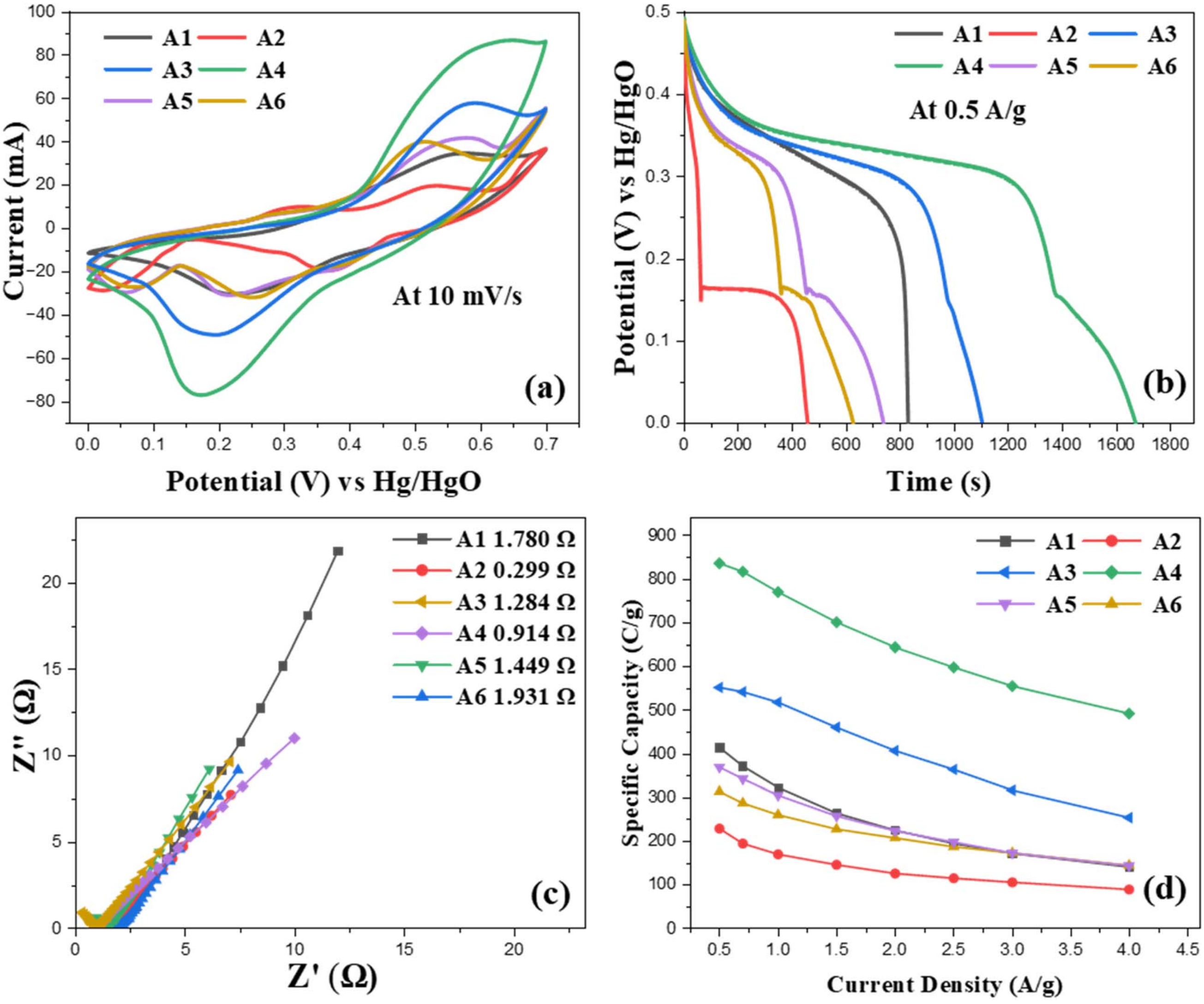

Fig. 7 Comparative electrochemical evaluation of samples A1–A6: (a) CV curves highlighting differences in redox activity; (b) GCD profiles showing variations in discharge durations; (c) Nyquist plots depicting equivalent series resistance, and (d) variation of Q_s with current density across the series.

displaying additional features associated with silver-citrate, which enhanced the current response. The incorporation of silver-citrate into the pristine sample introduces additional faradaic centers *via* Ag redox transitions and improves the electrical conductivity of the initial framework. With further optimization, Sample A4, as shown in Fig. 5(d), exhibited the highest current response and the broadest CV area, indicating improved charge storage capability. The improved electrochemical performance observed with increasing silver-citrate content is attributed to several synergistic effects. Uniformly distributed metallic Ag nanoparticles enhance electrical conductivity by forming highly conductive pathways that facilitate rapid electron transport. In addition, the reversible Ag^0/Ag_2O redox transitions provide extra faradaic contributions, complementing the intrinsic Ni^{2+}/Ni^{3+} and Co^{2+}/Co^{3+} redox activity of $NiCo_2S_4$.

However, further increasing the silver-citrate content beyond the optimal ratio of 40 percent in samples A5 and A6 in Fig. 5(e and f) resulted in a noticeable decrease in the CV redox peaks. This reduction in current response indicates reduced active surface accessibility and lower ion diffusion efficiency, likely due to agglomeration of Ag nanoparticles, a decrease in the mesoporosity of the calcined MOF composite, and a decrease in the relative proportion of the pristine $NiCo_2S_4$ phase. Consequently, sample A4 achieves an optimal balance of redox activity and electrical conductivity, delivering superior electrochemical performance among all tested compositions.

GCD analysis was conducted for samples A1–A6 to evaluate their electrochemical charge storage behavior quantitatively. As shown in Fig. 6, all samples exhibit non-linear GCD profiles recorded at current densities of 0.5–4 A g^{-1} within the 0–0.5 V potential window, suggesting the energy storage is predominantly governed by pseudocapacitive faradaic redox processes, in agreement with the CV observations. At lower current densities, the electrodes exhibited prolonged discharge times, indicating high charge storage capacity and rapid ion mobility within the electrode material.

With increasing current density, a gradual decrease in discharge duration was observed, attributable to diffusion-limited kinetics of electrolyte ions, which restrict redox activity primarily to the electrode's external surface. A moderate IR drop was observed, arising from the intrinsic internal resistance of the fabricated electrodes. However, the discharge curves remained smooth and reversible, indicating stable pseudocapacitive behavior. Sample A1, as shown in Fig. 6(a), exhibited sloped charge–discharge profiles consistent with its CV response, confirming the dominance of faradaic processes. In contrast, samples A2–A6 in Fig. 6(b–f) exhibited pronounced voltage plateaus corresponding to the redox peaks observed in their respective CV profiles. The characteristic voltage plateaus in the GCD curves confirm the reversible redox processes of silver-citrate within the composite matrix, affirming the battery-type charge-storage behavior of the composite electrodes.[48]

3.3.2 Comparison assessment of electrode materials. The comparative CV analysis at a 10 mV s^{-1} scan rate and GCD measurements at 0.5 A g^{-1} were employed, providing an appropriate balance between electrolyte-ion diffusion and surface-controlled processes. As shown in Fig. 7(a), all A1 electrodes exhibit redox peaks corresponding to the reversible redox behavior of transition-metal ions. The CV response exhibits quasi-rectangular profiles with well-characterized redox features, reflecting a hybrid charge-storage mechanism involving both EDLC response from the carbonaceous framework and faradaic pseudocapacitance from metal oxide and sulfide nanoparticles. Notably, sample A2 reveals the emergence of dual redox peaks, and subsequent composites with increasing silver-citrate content exhibit similar characteristics, indicating the additional contribution of silver-citrate redox processes. Among these, A4 exhibits the highest-intensity anodic and cathodic peaks, indicating superior electrochemical activity and enhanced charge storage capacity. The improved performance of A4 can be ascribed to the optimized silver-citrate content, which provides a synergistic balance between the conductive Ag species and the electroactive $NiCo_2S_4$ matrix, thereby enhancing electron transport and facilitating rapid ion diffusion across the electrode–electrolyte interface.

The CV findings are further corroborated by the GCD measurements shown in Fig. 7(b). Among the tested electrodes, A4 exhibits the longest discharge duration along with a distinct voltage plateau, consistent with CV observations and attributable to the presence of silver citrate. The long discharge plateau in the GCD curve reflects a shift in the dominant charge storage

Table 2 Electrochemical impedance parameters of samples A1–A6 obtained from Nyquist plot fitting

Electrode materials	ESR (Ω)	R_{ct} (Ω)	W_d (Ω)
A1	1.780	0.5044	0.0023
A2	1.448	1.147	0.0001783
A3	1.284	1.517	0.0005284
A4	0.914	0.208	0.02001
A5	1.449	1.591	0.000125
A6	1.931	0.5297	0.00252

Table 3 Comparative electrochemical performance of the siver-citrate/$NiCo_2S_4$/calcined MOFs with literature-reported electrodes

Material	Electrolyte	Specific capacitance/capacity	Current density	References
NiCoMn MOFs/silver-citrate	1 M KOH	730 F g^{-1}	0.5 A g^{-1}	45
$NiCo_2S_4$@carbon cloth	2 M KOH	879.6 F g^{-1}	1 A g^{-1}	49
NiCo MOF	3 M KOH	927.1 F g^{-1}	1 A g^{-1}	50
NiCoS	3 M KOH	922.06 F g^{-1}	0.62 A g^{-1}	51
Siver-citrate/$NiCo_2S_4$/calcined MOFs	1 M KOH	1678 F g^{-1}	0.5 A g^{-1}	This work

mechanism. In the initial portion of discharge, the rapid voltage decrease arises primarily from surface-controlled processes and IR drop, typical of capacitive and fast faradaic responses. Beyond the turning point, the relatively flat voltage plateau indicates the prevalence of battery-type faradaic redox processes, where the electrode undergoes sustained faradaic energy storage due to reversible redox reactions involving Ag species and transition-metal sulfides. This behavior is consistent with established mechanisms in hybrid and battery-type electrodes, where flat plateaus in GCD curves are recognized as signatures of bulk redox activity. In contrast, A5 and A6 display shorter discharge periods, suggesting limited ion diffusion, reduced utilization of electroactive sites, and a less porous framework available for electrolyte penetration. With the rise in current density from 0.5 to 4 A g^{-1}, all electrodes exhibit a gradual decrease in discharge time, reflecting diffusion-controlled kinetics in which charge storage primarily occurs at the electrode surface. These complementary CV and GCD results collectively confirm that the optimized incorporation of silver-citrate in A4 enhances electronic conductivity, promotes efficient ion transport, and results in superior overall electrochemical performance.

EIS analysis was conducted at 1–100,000 Hz frequency range to provide additional insight into interfacial resistance, charge-transfer kinetics, and diffusion properties. The Nyquist plots of samples A1–A6 are shown in Fig. 7(c). The equivalent series resistance (ESR), obtained from a through-equivalent circuit model, represents the collective contributions of the intrinsic resistance of the active material, the electrode–electrolyte interface, and the ionic resistance of the electrolyte. The ESR values for A1, A2, A3, A4, A5, and A6 were determined to be 1.780, 1.448, 1.284, 0.914, 1.449, and 1.931 Ω, respectively, with A4 exhibiting the lowest ESR, indicating its superior intrinsic conductivity and efficient ion transport. The reduced ESR and faster charge-transfer kinetics of A4 underscore its enhanced electrochemical performance.

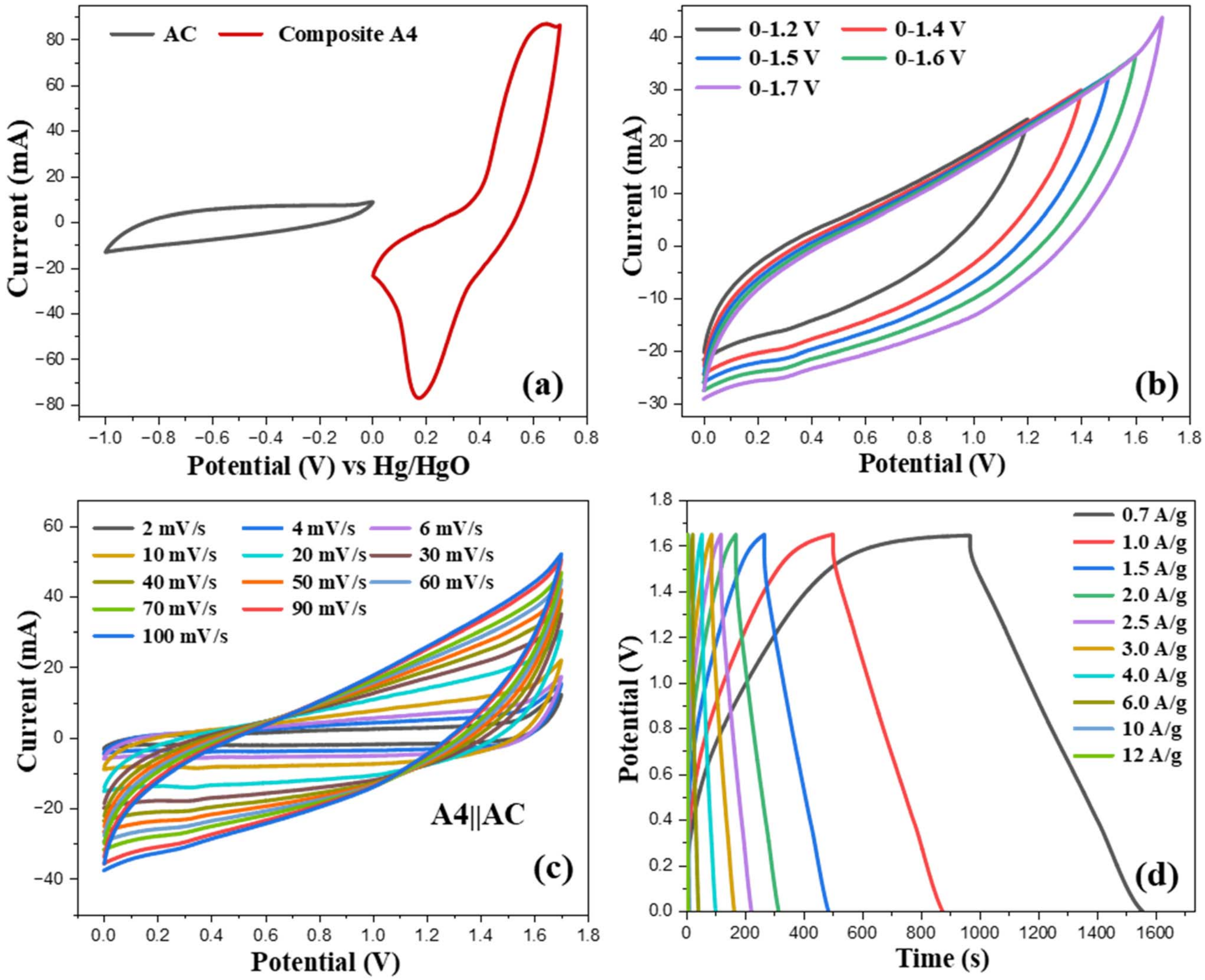

Fig. 8 Electrochemical performance of the A4||AC hybrid device: (a) CV curves of A4 and AC in a three-electrode setup at 10 mV s^{-1} (b) CVs under varying potential windows (0–1.2 V to 0–1.7 V) (c) CVs at scan rates of 2–100 mV s^{-1} and (d) GCD curves at different current densities within 0–1.65 V.

Further comparison of the charge-transfer resistance (R_{ct}) as shown in Table 2 values reveals that A4 also possesses the smallest R_{ct} (0.208 Ω), signifying faster electron transfer kinetics at the electrode–electrolyte interface. In contrast, samples A2, A3, and A5 exhibit relatively higher R_{ct} values (1.147–1.591 Ω), suggesting hindered faradaic reaction kinetics and inferior interfacial charge transfer. Although A1 and A6 show moderate R_{ct} values, their higher ESR limits overall electrochemical efficiency compared to A4. The Warburg diffusion resistance (W_d), which reflects ion diffusion behavior within the electrode structure, also varies notably among the samples. The relatively higher W_d value observed for A4 indicates pronounced diffusion-controlled behavior, which can be attributed to its hierarchical porous architecture that promotes deep electrolyte penetration and active ion diffusion throughout the electrode. For silver-citrate-modified composites, incorporation of silver-citrate effectively reduces the R_{ct} of pristine A1 due to the high electronic conductivity of Ag, thereby facilitating faster charge transfer. However, excessive silver-citrate loading leads to an increase in W_d, which is ascribed to partial pore blockage within the A1 framework, restricting ion diffusion pathways and increasing diffusion resistance. Overall, the synergistic combination of low ESR, minimal R_{ct}, and optimized diffusion characteristics endows sample A4 with superior charge transport and electrochemical kinetics, explaining its enhanced capacitive performance compared to the other electrodes.

The specific capacity (Q_s) of the synthesized electrodes was calculated from the GCD discharge profiles using eqn (i). As shown in Fig. 7(d), an inverse relationship between capacity and current density was observed, attributed to restricted ion diffusion and insufficient penetration of electrolyte ions into the internal active sites at high charge–discharge rates.

$$Q_s = \frac{I \times \Delta t}{m} \tag{i}$$

where Δt (s) is the discharge time, I (A) is the applied current and m (g) is active material mass. At 0.5 A g^{-1}, the specific capacities of samples A1–A6 were 414.5, 313.4, 369.5, 836, 552, and 229.15C g^{-1}, respectively. With the initial increase in silver-citrate content, the Q_s gradually increased, reaching a maximum at 40% silver-citrate (sample A4). Further addition

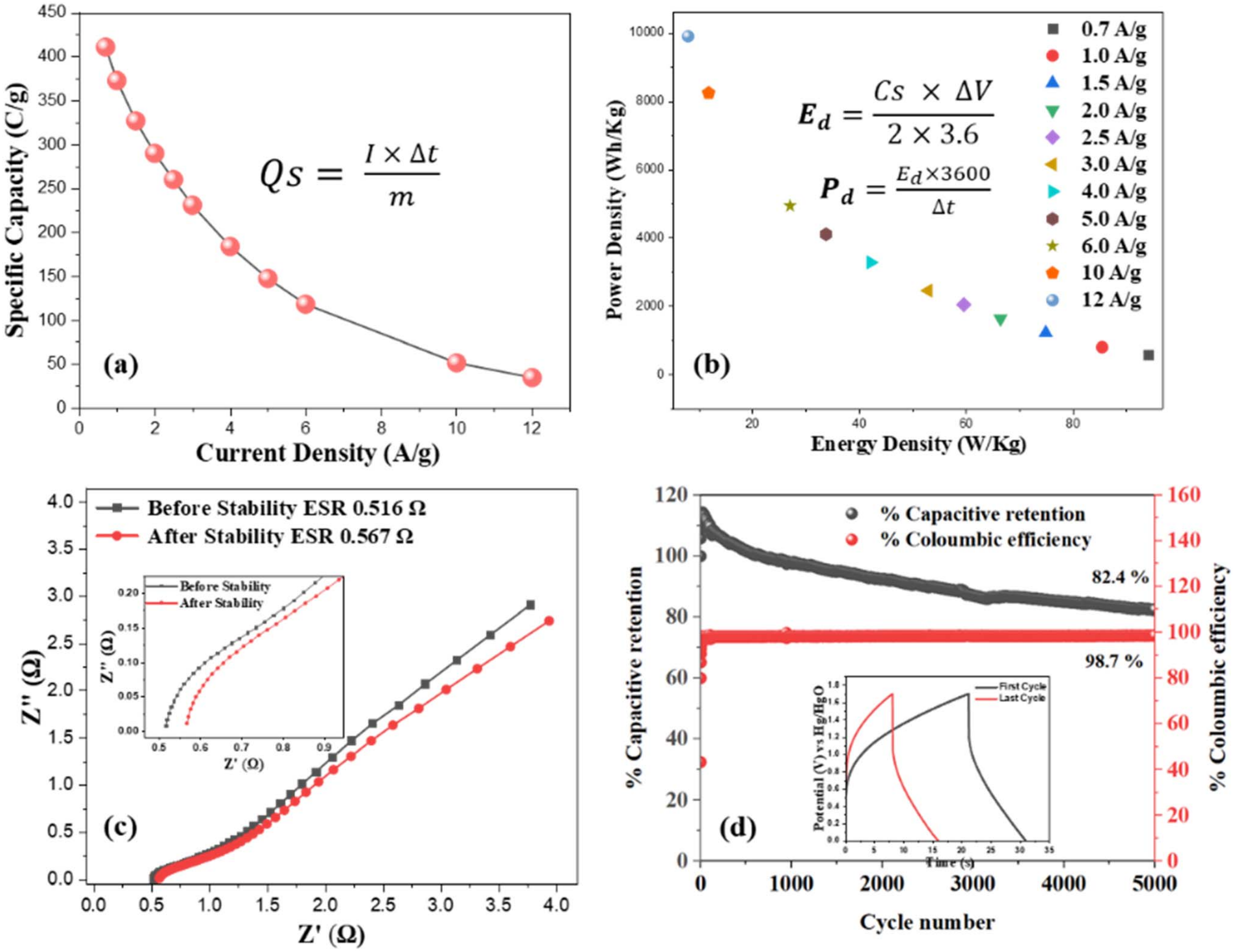

Fig. 9 Electrochemical performance of the A5||AC battery-type configurated hybrid device: (a) variation of Q_s with current density; (b) Ragone plot showing E_d *versus* P_d at various current densities; (c) Nyquist ploy recorded before and after cycling and (d) long-term cycling stability over 5000 cycles, showing coulombic efficiency and capacitance retention.

of silver-citrate in samples A5 and A6 resulted in a decline in Q_s, attributed to the reduced contribution of the calcined MOFs framework and decreased sulfide content in these compositions. Among all samples, A4 exhibited the highest Q_s and maintained superior performance at higher current densities, due to the optimal synergistic interaction between $NiCo_2S_4$, the MOF-derived conductive carbon framework, and the appropriately balanced silver-citrate content. A comparison of capacitance achieved for our optimized sample with previous literature have been done in Table 3.

3.3.3 Electrochemical performance of the assembled siver-citrate-incorporated $NiCo_2S_4$/NiCoZn oxide@carbon||AC device.

The evaluation of A4's electrochemical performance was conducted using an asymmetric supercapacitor configuration, where A4 functioned as the cathode, and AC was utilized as the anode in 1 M KOH aqueous solution. A Hoffman filter paper (permeable membrane) was used between these electrodes to facilitate the transport of electrolyte ions. Initially, the charge-storage mechanisms of both electrodes were compared using a three-electrode configuration, as illustrated in Fig. 8(a). CV of an AC electrode was conducted within a potential window of 0 to −1 V, and the resulting voltammogram exhibited a quasi-rectangular shape, characteristic of electric double-layer capacitive behavior. In contrast, the CV of A4, recorded between 0 and 0.7 V, exhibited well-defined redox peaks, indicating pseudocapacitive behavior.

The cyclic voltammogram of the assembled supercapacitor device, denoted as silver-citrate-$NiCo_2S_4$/NiCoZn oxide@carbon||AC, is depicted in Fig. 8(b). Initially, cyclic voltammetry measurements were performed at progressively increasing potential windows, from 0–1.2 V to 0–1.7 V, to identify the optimal operating range of the device. The curves revealed an increase of the potential window to 1.7 V, accompanied by a noticeable increase in the enclosed area, signifying enhanced energy storage capability. Subsequent CV scans, recorded within 0–1.7 V at scan rates from 2 to 100 mV s^{-1} as depicted in Fig. 8(c), displayed features characteristic of both capacitive and pseudocapacitive behaviors. A nearly rectangular capacitive contribution up to 0.6 V corresponded to the EDLC of the AC electrode, while the redox peaks beyond 0.4 V reflected the faradaic contribution of A4. The CV profiles upheld symmetric response even at higher scan rates, confirming the device's excellent electrochemical stability and rate performance.

Following the CV assessment, GCD measurements were performed to evaluate the charge storage performance and energy storage capacity within the potential window 0–1.65 V at current densities of 0.7 to 12 A g^{-1}, as illustrated in Fig. 8(d). The GCD profiles exhibit a non-linear, asymmetric shape, reflecting the coexistence of EDLC and faradaic redox contributions. A small voltage plateau is observed, particularly at lower current densities, corresponding to reversible redox transitions associated with the battery-type A4 electrode. A minor initial voltage drop (IR drop) is noticeable, suggesting low internal resistance and good electrical contact within the device. As the current density increases, the discharge duration decreases while the overall curve shape remains well preserved, highlighting efficient charge–discharge reversibility.

The A4||AC device achieved a high Q_s of 411.6C g^{-1} at 0.7 A g^{-1}. Even at an elevated current density of 12 A g^{-1}, it retained a considerable capacity of 55C g^{-1}, as depicted in Fig. 9(a). This retention demonstrates superior rate capability, suggesting that the integrated calcined MOF porous framework and the conductive network of the sulfide and silver-citrate complex in A4 effectively facilitate rapid ion diffusion and electron transport, ensuring robust electrochemical stability during repeated cycling. The assembled A4||AC device was further analyzed by calculating its E_d and P_d using eqn (ii) and (iii). These results were then represented in a Ragone plot, as depicted in Fig. 9(b) to illustrate the device's energy-power characteristics.

$$E_d = \frac{Q_s \times \Delta V}{2 \times 3.6} \tag{ii}$$

$$P_d = \frac{E_d \times 3600}{\Delta t} \tag{iii}$$

The supercapacitor's device delivered a notable E_d of 94 Wh kg^{-1} with a corresponding P_d of 577 W kg^{-1} at 0.7 A g^{-1}. Impressively, even at an elevated current density of 12 A g^{-1}, the device sustained an E_d of 8 Wh kg^{-1} while achieving a high P_d of 10 kW kg^{-1}. In energy storage systems, E_d and P_d are inversely related, such that higher energy storage is achieved at lower power output, while rapid energy delivery at high power often results in reduced E_d. This behavior is attributed to the inherent balance between energy and power. When the current density is low, ions have sufficient time to intercalate into the porous electrode structure. This allows the device to utilize almost all active material, maximizing E_d. However, since the discharge is slower, the power output appears lower. At high current densities, energy is delivered rapidly through readily accessible active sites, resulting in higher power output but lower energy utilization.

To assess the impact of prolonged cycling on the device's performance, EIS measurements were conducted both before and after the stability tests to evaluate the device's internal resistance and charge-transfer characteristics. Both curves exhibit a small intercept on the real axis, indicative of a low ESR, which facilitates rapid charge transport and efficient ion diffusion, as reflected in the higher Q_s of the A4 electrode compared to the other samples. The ESR shows a negligible increase from 0.516 Ω before cycling to 0.561 Ω after prolonged cycling, due to minor surface passivation. These low ESR values confirm the excellent electronic conductivity and strong interfacial contact of the electrodes. The R_{ct} determined from the high-frequency semicircle remains unchanged mainly after cycling, whereas the low-frequency tail becomes slightly more inclined toward the *x*-axis, indicating minor variations in Warburg diffusion behavior. Lastly, we examined the supercapacitor device over 5000 GCD cycles to evaluate its coulombic efficiency and long-term stability. Fig. 9(d) presents the assessment, which revealed that the device retained a substantial 82.4% capacitance and a high coulombic efficiency of 98.7% throughout the extended cycling period. These findings demonstrate the robust cyclic durability of the fabricated device.

3.3.4 Reaction mechanism in silver-citrate/NiCo$_2$S$_4$@-calcined MOF composite. The charge storage behavior of the silver-citrate modified NiCo$_2$S$_4$@calcined-MOF electrode appeared by combined contribution from an EDLC due to carbonaceous framework and faradaic pseudocapacitance originating from the MOF-derived metal oxides, *in situ* grown NiCo sulfides, and silver ions. At high scan rates and current densities, the charge storage process is mainly dominated by surface-controlled capacitive behavior. At lower scan rates and current densities, faradaic redox reactions involving MOF-derived metal oxides and sulfides become dominant. During calcination, the NiCoZn-MOF is transformed into a mixed-metal oxide-carbon framework, where Ni- and Co-based oxides provide abundant redox-active sites. In alkaline electrolyte, these oxides undergo reversible redox transitions, contributing pseudocapacitive charge storage according to the following reactions:[52]

$$\mathrm{NiO} + \mathrm{OH}^- \leftrightarrow \mathrm{NiOOH} + \mathrm{e}^-$$

$$\mathrm{CoO} + \mathrm{OH}^- \leftrightarrow \mathrm{CoOOH} + \mathrm{e}^-$$

Simultaneously, the *in situ* grown NiCo$_2$S$_4$ nanostructures exhibit shows reversible redox transitions of Ni and Co species within the sulfide lattice:[53]

$$\mathrm{NiCo_2S_4} + 2\mathrm{OH}^- \leftrightarrow \mathrm{NiSOH} + \mathrm{CoSOH} + 2\mathrm{e}^-$$

The incorporation of silver-citrate introduces additional redox centers, further enriching the faradaic contribution:[45]

$$\mathrm{Ag} + \mathrm{OH}^- \leftrightarrow \mathrm{AgOH} + \mathrm{e}^-$$

Beyond contributing redox activity, Ag species significantly enhance electronic conductivity and reduce charge-transfer resistance, enabling more synchronized and reversible redox reactions throughout the electrode and suppressing polarization effects. Moreover, the calcined MOF-derived oxide-carbon framework serves as a robust structural scaffold, accommodating volume changes associated with repeated redox cycling of oxides, sulfides, and Ag species. The hierarchical porous architecture shortens ionic diffusion pathways, ensures efficient electrolyte penetration, and prevents particle agglomeration, thereby maintaining excellent cycling stability.

3.3.5 Comparison with literature. The A4||AC assembled device investigated in this study demonstrates superior performance in comparison with the other supercapacitor devices listed in Table 4. For instance, a previous study on NiCoMn MOF/silver-citrate composites reported an E_d of 61 Wh kg^{-1} at a P_d of 1500 W kg^{-1}.[45] In contrast, our strategy, in which MOFs are first transformed into an oxide-carbon framework, followed by the *in situ* growth of sulfide species and subsequent compositing with silver-citrate, significantly enhances energy storage performance. This integrated design elevates the E_d to 94 Wh kg^{-1} at a P_d of 577 W kg^{-1}, demonstrating the superior electrochemical advantages achieved through structural optimization and synergistic interactions within the composite. These results highlight the critical role of silver-citrate-NiCo$_2$S$_4$/NiCoZn Oxide@Carbon nanocomposites in advancing supercapacitor technology. Unlike conventional composites, our approach first enhanced the stability of the MOFs structure through calcination, then leveraged the porous morphology of the calcined MOFs to grow sulfide nanoparticles, improving conductivity. Finally, the incorporation of silver-citrate further

Table 4 Summary of reported cathode||anode hybrid supercapacitor systems, highlighting synthesis routes, material morphologies, and their corresponding energy and power densities

Cathode‖anode	Synthesis route	Morphology	E_d (Wh kg^{-1}) and P_d (W kg^{-1})	References
NiCoMn MOFs/silver-citrate‖AC	Ultrasonication-assisted solvothermal	Spherical silver-citrate incorporated into MOFs sheets	61/1500	45
NiCoZn-LDH‖AC	Template-assisted (using CoZn-MOFs precursor)	Hollow dodecahedron	65.66/368.21	54
NiCo-MOFs‖AC	Ultrasonication-assisted synthesis	Ultrathin nanosheets	49.4/562.5	55
Ni–Zn hydroxide/rGO‖AC	MOFs template	Ultrathin nanosheets, sandwich-like, vertically aligned on rGO	53.7/825.1	56
MnO$_2$@NiCoZn–OH‖AC	MOFs-template route	Hollow MnO$_2$ nanotubes coated with NiCoZn–OH nanosheets	49.4/842.7	57
NiO/C/rGO‖AC derived from sodium citrate	Pyrolysis of Ni-MOFs with graphene oxide	NiO nanoparticles dispersed on rGO	35.9/749.1	35
NCA15-MOF/NF‖AC	Solvothermal method	Spherical	72.55/408.61	58
silver-citrate/NiCo$_2$S$_4$@calcined MOFs composite	Hydrothermal synthesis of the MOFs, followed by calcination, enabled the formation of a porous framework that subsequently supported the *in situ* growth of sulfide nanoparticles, followed incorporation of silver-citrate	A plate-like calcined MOFs architecture decorated with NiCo$_2$S$_4$ nanoparticles and uniformly dispersed spherical silver-citrate species	94/577	This work

enhanced both the charge storage capacity and cycling stability of the device. These results offer valuable insights for optimizing charge storage performance, long-term stability, and overall efficiency in supercapacitor systems.

3.3.6 Capacitive and diffusive nature analysis. The electrochemical charge-storage behavior of the A4‖AC hybrid device was further investigated by quantifying the contributions of capacitive and diffusion processes. For this purpose, Dunn's method was applied to the CV current response, which allows the current response to be separated into surface-limited (capacitive) and diffusion-dependent (Faradaic) components.[59] The overall current response $i_{(\mathrm{V})}$ of the actual device arises from the combined contributions of faradaic reactions, governed by electrolyte-ion diffusion $i_{(\mathrm{F})}$, and surface-limited non-faradaic (capacitive) processes $i_{(\mathrm{nF})}$.

$$i_{(\mathrm{V})} = i_{(\mathrm{F})} + i_{(\mathrm{nF})} \qquad \text{(iv)}$$

$$i_{(\mathrm{V})} = i_{(\mathrm{F})} + i_{(\mathrm{nF})} = K_\mathrm{a}v + K_\mathrm{b}v^{1/2} \qquad \text{(v)}$$

where, $K_\mathrm{a}v$ denotes the surface-controlled component, while $K_\mathrm{b}v^{1/2}$ denotes diffusion-governed charge storage.[60] The analysis at a 10 mV s^{-1} scan rate revealed that approximately 36% of the stored charge originates from capacitive processes, whereas 64% arises from faradaic redox reactions.

The $NiCo_2S_4$ nanoparticles act as the dominant faradaic centers, where the multivalent Ni and Co species undergo reversible redox transitions. In addition, the metallic Ag present in the silver-citrate composite also participates in a redox charge-storage mechanism through its Ag^0/Ag^+ redox couple, further enhancing the faradaic contribution. In contrast, the citrate groups primarily facilitate non-faradaic ion adsorption through their polar $-COO^-$ functionalities, thereby increasing the capacitive response. Significant capacitive behavior originates from the AC negative electrode, which promotes rapid electrostatic ion accumulation at the electrode–electrolyte

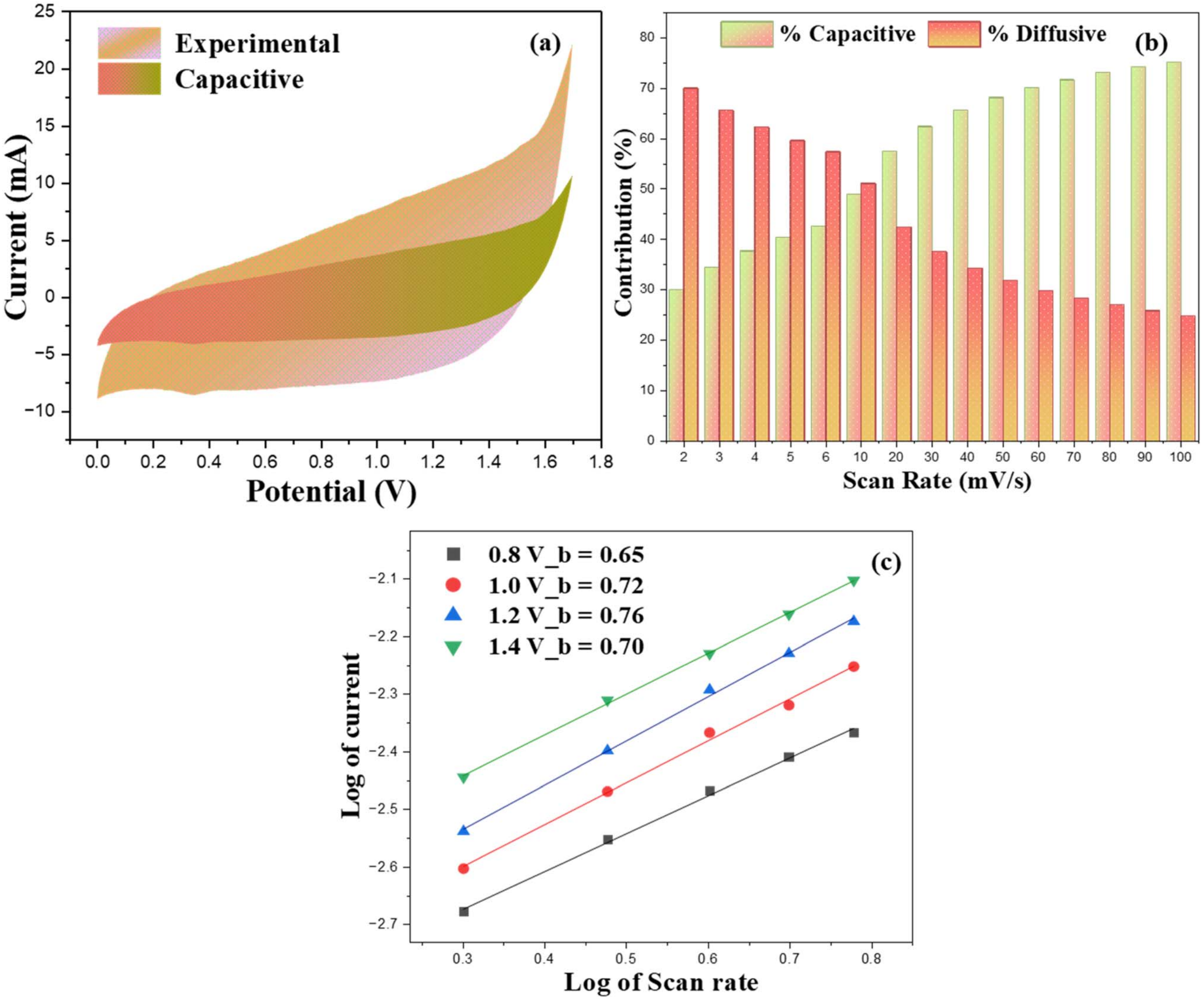

Fig. 10 Capacitive and diffusion-controlled charge storage in the A4‖AC device: (a) CV at 10 mV s^{-1} with the green-shaded area showing capacitive contribution; (b) variation of capacitive and diffusion contributions with scan rate; (c) log(i)–log(v) plots for b-value determination.

interface. Collectively, these synergistic contributions define the hybrid charge-storage mechanism.

The CV curve in Fig. 10(a) highlights the capacitive region as a gradient of green within the total current profile. The variation in charge-storage contributions at different scan rates is summarized in Fig. 10(b), which shows an increase in capacitive behavior with increasing scan rate. At low scan rates, electrolyte ions can effectively penetrate into the electrode material, allowing $NiCo_2S_4$ sulfide nanoparticles and metallic Ag to undergo diffusion-controlled faradaic redox reactions that dominate charge storage. Conversely, at higher scan rates, limited ion transport into the electrode structure confines the electrochemical processes to the electrode surface. Therefore, capacitive contributions become more pronounced, arising from the MOF-derived carbon framework and the polar citrate groups in the silver-citrate composite, which facilitate surface ion adsorption. This synergy between charge accumulation at the electrode surface and Faradaic processes confirms the hybrid charge-storage nature of the A5||AC device and highlights the synergistic interplay among its multiple components in achieving both rapid charge–discharge performance and high capacity.

To further investigate the dominant charge-storage mechanism, the relationship between the log of the peak current (log i) and the log of the scan rate (log v) was analyzed in ref. 61:

$$i = av^b \tag{vi}$$

In the log(i)–log(v) analysis, a b-value of 0.5 represents diffusion-controlled behavior, while values approaching 1.0 indicate surface-controlled capacitive processes. For the A4||AC electrode, the extracted b-values range from 0.65 to 0.76 (Fig. 10(c)), indicating that the charge storage involves a combination of capacitive and faradaic contributions. This dual mechanism indicates the hybrid nature of the electrode, in which the coexistence of electrostatic and faradaic behavior underpins its enhanced charge storage performance.

4 Conclusion

In summary, we have developed an silver-citrate-incorporated $NiCo_2S_4$@calcined-MOF composite using a trimetallic NiCoZn-TPA MOF as a versatile precursor for high-performance hybrid supercapacitor electrodes. Calcination of the NiCoZn MOF produced a porous NiO/CoO/ZnO/carbon framework that combines structural robustness with enhanced electrical conductivity. This framework acted as an efficient template for the *in situ* growth of $NiCo_2S_4$ nanoparticles, providing abundant redox-active sites while maintaining good ion-accessible porosity. Subsequent incorporation of silver-citrate introduced additional pseudocapacitive centers and highly conductive Ag pathways, while the citrate ligand contributed to structural stabilization and improved surface wettability. Structural and morphological analyses confirmed the coexistence and uniform distribution of the oxide-carbon matrix, $NiCo_2S_4$, and silver-citrate within a plate-like composite architecture. Among the series of samples, the optimized composition A4 (60 wt% $NiCo_2S_4$@calcined-MOFs/40 wt% silver-citrate) exhibited the lowest equivalent series resistance and the most pronounced redox response. In a three-electrode configuration, A4 delivered a high specific capacity of ~836C g^{-1} at 0.5 A g^{-1}, indicating efficient utilization of the multicomponent active network. When assembled in an asymmetric configuration with activated carbon (A4//AC), the device operated stably up to 1.7 V in 1 M KOH and achieved an energy density of ~94 Wh kg^{-1} at a power density of ~577 W kg^{-1}. The device maintained high-rate capability at elevated current densities and retained approximately 82% of its initial capacitance after 5000 charge–discharge cycles, with a coulombic efficiency close to 98%. Dunn analysis and b-value fitting revealed a mixed charge-storage mechanism, with both diffusion-controlled faradaic processes and surface-controlled capacitive contributions, consistent with the hybrid nature of the electrode design. Furthermore, this work demonstrates that coupling MOF-derived oxide-carbon frameworks with transition-metal sulfides and silver-citrate is an effective strategy to enhance conductivity, redox activity, and cycling stability simultaneously. Future efforts can focus on optimizing the metal combinations, silver-citrate content, and device engineering (including flexible and solid-state formats) to advance further the performance and practical applicability of this class of hybrid supercapacitor materials.

Author contributions

Areeba Sajid: conceptualization, methodology, formal analysis, software, writing – original draft, data curation Mohsin Ali Marwat: conceptualization, investigation, writing – review & editing, supervision, funding acquisition, project administration Hamza Mohsin: writing – original draft, supervision, visualization, writing – review & editing Syed Shaheen Shah: software, writing – review & editing, visualization. Muhammad Arqam Karim: software, visualization, formal analysis, review & editing, Muhammad Tariq: visualization, review & editing, Zuhair Ehsan: formal analysis, writing – original draft, Anusha Arif: visualization, review & editing.

Conflicts of interest

The authors declare that they have no known competing financial interests or personal relationships that could have appeared to influence the work reported in this paper.

Data availability

The data that supports the findings of this study are available upon reasonable request.

Supplementary information (SI) is available. See DOI: https://doi.org/10.1039/d5ra09122e.

Acknowledgements

M. A. Marwat acknowledges the valuable academic and research support from Pakistan Science Foundation (PSF) Project No. PSF-NSFC/202307/19 and Ghulam Ishaq Khan (GIK) Institute of

Engineering Sciences and Technology. Thanks for the financial support of the National Natural Science Foundation of China (No. 22461142142, U24A20203).

References

1 C. Li, *et al.*, MOF-derived NiZnCo-P nano-array for asymmetric supercapacitor, *Chem. Eng. J.*, 2022, **446**, 137108.
2 R. R. Salunkhe, *et al.*, Fabrication of symmetric supercapacitors based on MOF-derived nanoporous carbons, *J. Mater. Chem. A*, 2014, **2**(46), 19848–19854.
3 G. Nagaraju, *et al.*, High-performance hybrid supercapacitors based on MOF-derived hollow ternary chalcogenides, *Energy Storage Mater.*, 2021, **35**, 750–760.
4 J. Libich, *et al.*, Supercapacitors: Properties and applications, *J. Energy Storage*, 2018, **17**, 224–227.
5 B. E. Conway, V. Birss and J. Wojtowicz, The role and utilization of pseudocapacitance for energy storage by supercapacitors, *J. Power Sources*, 1997, **66**(1), 1–14.
6 N. Zhang, I. Amorim and L. Liu, Multimetallic transition metal phosphide nanostructures for supercapacitors and electrochemical water splitting, *Nanotechnology*, 2022, **33**(43), 432004.
7 Y. Gao and L. Zhao, Review on recent advances in nanostructured transition-metal-sulfide-based electrode materials for cathode materials of asymmetric supercapacitors, *Chem. Eng. J.*, 2022, **430**, 132745.
8 B. Xu, *et al.*, Recent progress in metal-organic framework-based supercapacitor electrode materials, *Coord. Chem. Rev.*, 2020, **420**, 213438.
9 D.-G. Wang, *et al.*, Metal-organic framework-based materials for hybrid supercapacitor application, *Coord. Chem. Rev.*, 2020, **404**, 213093.
10 S. Sharma, P. Chand and S. Kaushik, A critical review of recent advancements in zinc based metal organic framework nanocomposites and their derivatives for supercapacitor applications with future perspectives and challenges, *Sustainable Mater. Technol.*, 2024, **41**, e01045.
11 M. A. Karim, *et al.*, Electrochemical insights into NiCoCu-based MOFs for energy storage applications, *Electrochim. Acta*, 2025, **542**, 147509.
12 I. Arshad, *et al.*, Enhanced electrochemical performance of NiCoMn MOFs with Ag-citrate/SWCNT nanocomposites for high-energy supercapacitors, *Diamond Relat. Mater.*, 2025, **155**, 112246.
13 V. Shrivastav, *et al.*, Metal-organic frameworks-derived titanium dioxide–carbon nanocomposite for supercapacitor applications, *Int. J. Energy Res.*, 2020, **44**(8), 6269–6284.
14 V. Shrivastav, *et al.*, Metal-organic framework derived zirconium oxide/carbon composite as an improved supercapacitor electrode, *Energy*, 2021, **235**, 121351.
15 C. Hu, *et al.*, Tailor-made overstable 3D carbon superstructures towards efficient zinc-ion storage, *Chin. Chem. Lett.*, 2025, **36**(4), 110381.
16 P. D. Patil, *et al.*, Effect of annealing temperature on morphologies of metal organic framework derived NiFe2O4 for supercapacitor application, *J. Energy Storage*, 2021, **40**, 102821.
17 A. Sajid, Y. Sohail and M. A. Marwat, FeNiS/PANI Hybrid Composite for Enhanced Electrochemical Energy Storage Performance, *Mater. Proc.*, 2025, **23**, 22, DOI: 10.3390/materproc2025023022.
18 J. Rehman, *et al.*, Engineering of Transition Metal Sulfide Nanostructures as Efficient Electrodes for High-Performance Supercapacitors, *ACS Appl. Energy Mater.*, 2022, **5**(6), 6481–6498.
19 Y. Gu, *et al.*, Metal-organic framework-derived transition metal sulfides promote the development of high-performance supercapacitors, *J. Energy Storage*, 2025, **140**, 119008.
20 S. Wu, *et al.*, A review of performance optimization of MOF-derived metal oxide as electrode materials for supercapacitors, *Int. J. Energy Res.*, 2019, **43**(2), 697–716.
21 L. Yuan, *et al.*, Facial Synthesis of Silver-incorporated Conductive Polypyrrole Submicron Spheres for Supercapacitors, *Electrochim. Acta*, 2016, **213**, 115–123.
22 S. Khamlich, *et al.*, Rapid microwave-assisted growth of silver nanoparticles on 3D graphene networks for supercapacitor application, *J. Colloid Interface Sci.*, 2017, **493**, 130–137.
23 S. Ali, *et al.*, Ag NPs-modified NiCoMn layered double hydroxides electrodes for high-performance asymmetric supercapacitors, *J. Alloys Compd.*, 2024, **1008**, 176865.
24 W.-Q. Zhang, *et al.*, Effect of Coordinated Solvent Molecules on Metal Coordination Sphere and Solvent-Induced Transformations, *Cryst. Growth Des.*, 2017, **17**(2), 517–526.
25 K. B. Nilsson, M. Maliarik and I. Persson, Coordination Chemistry of Solvated Metal Ions in Soft Donor Solvents, *Molecules*, 2025, **30**, 3063, DOI: 10.3390/molecules30153063.
26 N. K. Gupta, Terephthalate and trimesate metal–organic frameworks of Mn, Co, and Ni: exploring photostability by spectroscopy, *RSC Adv.*, 2021, **11**(15), 8951–8962.
27 C. Hu, *et al.*, MOF derived ZnO/C nanocomposite with enhanced adsorption capacity and photocatalytic performance under sunlight, *J. Hazard. Mater.*, 2020, **385**, 121599.
28 T. Q. N. Tran, *et al.*, Metal–organic framework–derived Ni@C and NiO@C as anode catalysts for urea fuel cells, *Sci. Rep.*, 2020, **10**(1), 278.
29 Q. Zhou, Y. Gong and K. Tao, Calcination/phosphorization of dual Ni/Co-MOF into NiCoP/C nanohybrid with enhanced electrochemical property for high energy density asymmetric supercapacitor, *Electrochim. Acta*, 2019, **320**, 134582.
30 C. Dong, *et al.*, Copper sulfide for high-rate and long-life sodium storage through conversion–displacement chemistry, *Chem. Eng. J.*, 2025, **514**, 163349.
31 Q. Huo, *et al.*, Adsorption desulfurization performances of Zn/Co porous carbons derived from bimetal-organic frameworks, *Chem. Eng. J.*, 2019, **362**, 287–297.
32 S. Xu, *et al.*, ZIF-derived nitrogen-doped porous carbons as highly efficient adsorbents for removal of organic compounds from wastewater, *Chem. Eng. J.*, 2017, **323**, 502–511.

33 K. Huang, *et al.*, MOF-assisted synthesis of Ni, Co, Zn, and N multidoped porous carbon as highly efficient oxygen reduction electrocatalysts in Zn–air batteries, *Mater. Today Energy*, 2021, **19**, 100579.

34 K. M. Nam, *et al.*, Syntheses and Characterization of Wurtzite CoO, Rocksalt CoO, and Spinel Co3O4 Nanocrystals: Their Interconversion and Tuning of Phase and Morphology, *Chem. Mater.*, 2010, **22**(15), 4446–4454.

35 Z. Zhang, *et al.*, Ni-MOF derived NiO/C nanospheres grown in situ on reduced graphene oxide towards high performance hybrid supercapacitor, *J. Alloys Compd.*, 2019, **801**, 158–165.

36 P. J. Jodłowski, *et al.*, In situ deposition of M(M=Zn; Ni; Co)-MOF-74 over structured carriers for cyclohexene oxidation - Spectroscopic and microscopic characterisation, *Microporous Mesoporous Mater.*, 2020, **303**, 110249.

37 Y. Zhu, *et al.*, Mesoporous NiCo2S4 nanoparticles as high-performance electrode materials for supercapacitors, *J. Power Sources*, 2015, **273**, 584–590.

38 M. Sakthivel, *et al.*, Synthesis and characterization of bimetallic nickel-cobalt chalcogenides (NiCoSe2, NiCo2S4, and NiCo2O4) for non-enzymatic hydrogen peroxide sensor and energy storage: Electrochemical properties dependence on the metal-to-chalcogen composition, *Renew. Energy*, 2019, **138**, 139–151.

39 K. M. Adam, *et al.*, Battery-grade silver citrate-nickel hydroxide-multiwalled carbon nanotubes nanocomposites for high-performance supercapattery applications, *J. Energy Storage*, 2024, **81**, 110448.

40 M. R. Das, *et al.*, The synthesis of citrate-modified silver nanoparticles in an aqueous suspension of graphene oxide nanosheets and their antibacterial activity, *Colloids Surf., B*, 2013, **105**, 128–136.

41 Y. Ma, *et al.*, Trimetallic metal–organic framework nanosheets as nanozymes for the electrochemical sensing of H2O2, *J. Electroanal. Chem.*, 2023, **940**, 117490.

42 S. Rai, *et al.*, Synthesis, characterizations, and electrochemical studies of ZnO/reduced graphene oxide nanohybrids for supercapacitor application, *Mater. Today Chem.*, 2021, **20**, 100472.

43 M. Mazaj, *et al.*, Spectroscopic Studies of Structural Dynamics Induced by Heating and Hydration: A Case of Calcium-Terephthalate Metal-Organic Framework, *J. Phys. Chem. C*, 2013, **117**, 7552–7564.

44 X. Liang, *et al.*, In-situ growth of bimetallic sulfide NiCo2S4 nanowire on carbon cloth for asymmetric flexible supercapacitors, *J. Energy Storage*, 2021, **42**, 103105.

45 M. A. Marwat, *et al.*, Novel NiCoMn MOFs/Ag citrate nanocomposites for high-performance asymmetric supercapacitor applications, *Electrochim. Acta*, 2025, **511**, 145373.

46 J.-H. Zhong, *et al.*, Co3O4/Ni(OH)2 composite mesoporous nanosheet networks as a promising electrode for supercapacitor applications, *J. Mater. Chem.*, 2012, **22**(12), 5656–5665.

47 A. I. Oje, *et al.*, Pseudo-capacitance of silver oxide thin film electrodes in ionic liquid for electrochemical energy applications, *J. Sci.:Adv. Mater. Devices*, 2019, **4**(2), 213–222.

48 R. E. El Shater, *et al.*, Electrochemical investigation of Ag mixed Cd–Cu nanoferrite mixed reduced graphene oxide as improved platform for supercapacitor application, *J. Mater. Sci.: Mater. Electron.*, 2023, **34**(9), 842.

49 D. Wang, *et al.*, "One for two" strategy to prepare MOF-derived NiCo2S4 nanorods grown on carbon cloth for high-performance asymmetric supercapacitors and efficient oxygen evolution reaction, *Electrochim. Acta*, 2020, **334**, 135636.

50 Y. Du, *et al.*, High-performance quasi-solid-state flexible supercapacitors based on a flower-like NiCo metal-organic framework, *RSC Adv.*, 2022, **12**(10), 5910–5918.

51 S. S. Rao, Hierarchical nanospheres of NiCoS/NF for high-performance supercapacitors, *Nano-Struct. Nano-Objects*, 2019, **19**, 100366.

52 Y. Shao, *et al.*, Design and Mechanisms of Asymmetric Supercapacitors, *Chem. Rev.*, 2018, **118**(18), 9233–9280.

53 G. B. Pour, *et al.*, Recent advances in Ni-materials/carbon nanocomposites for supercapacitor electrodes, *Mater. Adv.*, 2023, **4**(23), 6152–6174.

54 Z. Lin, *et al.*, Fabrication of the hollow dodecahedral NiCoZn layered double hydroxide for high-performance flexible asymmetric supercapacitor, *J. Colloid Interface Sci.*, 2024, **657**, 91–101.

55 Y. Wang, *et al.*, Ultrathin NiCo-MOF Nanosheets for High-Performance Supercapacitor Electrodes, *ACS Appl. Energy Mater.*, 2019, **2**(3), 2063–2071.

56 Y. Du, *et al.*, Sandwich-like Ni-Zn hydroxide nanosheets vertically aligned on reduced graphene oxide via MOF templates towards boosting supercapacitive performance, *Chem. Eng. J.*, 2021, **417**, 129189.

57 Y. Du, *et al.*, Core–Shell MnO2 Nanotubes@Nickel–Cobalt–Zinc Hydroxide Nanosheets for Supercapacitive Energy Storage, *ACS Appl. Nano Mater.*, 2020, **3**(8), 7462–7473.

58 C. Chu, *et al.*, Silver-incorporated NiCo metal–organic frameworks with controlled morphology for enhanced cycling in flexible supercapacitor applications, *J. Mater. Chem. C*, 2025, **13**(2), 743–757.

59 S. Dubal, *et al.*, Polyacrylonitrile-based carbon nanofiber electrode fabricated via electrospun for supercapacitor application, *Proc. Inst. Mech. Eng., Part N: J. Nanoeng. Nanosyst.*, 2024, 23977914241232161.

60 R. Kumar and M. Bag, Quantifying Capacitive and Diffusion-Controlled Charge Storage from 3D Bulk to 2D Layered Halide Perovskite-Based Porous Electrodes for Efficient Supercapacitor Applications, *J. Phys. Chem. C*, 2021, **125**(31), 16946–16954.

61 F. J. Mascarenhas, *et al.*, Electrodeposited CoMnS/NiCo2S4 nanocomposite for high performance supercapacitors, *Electrochim. Acta*, 2024, **507**, 145133.